Lawrence Berkeley National Laboratory
LBL Publications

Title

Interactive roles of geometrical distribution and geomechanical deformation of fracture networks in fluid flow through fractured geological media

Permalink

https://escholarship.org/uc/item/5c39668b

Journal

Journal of Rock Mechanics and Geotechnical Engineering, 12(4)

ISSN

1674-7755

Authors

Lei, Qinghua
Wang, Xiaoguang
Min, Ki-Bok
et al.

Publication Date

2020-08-01

DOI

10.1016/j.jrmge.2019.12.014

Peer reviewed

eScholarship.org Powered by the California Digital Library
University of California

Journal of Rock Mechanics and Geotechnical Engineering 12 (2020) 780–792

Contents lists available at ScienceDirect

Journal of Rock Mechanics and Geotechnical Engineering

journal homepage: www.jrmge.cn

Full Length Article

Interactive roles of geometrical distribution and geomechanical deformation of fracture networks in fluid flow through fractured geological media

Qinghua Lei [a], Xiaoguang Wang [b,*], Ki-Bok Min [c], Jonny Rutqvist [d]

[a] Department of Earth Sciences, ETH Zürich, Zürich, Switzerland
[b] Laboratoire HydroSciences Montpellier, Université de Montpellier, Montpellier, France
[c] Department of Energy Systems Engineering, Seoul National University, Seoul, Republic of Korea
[d] Energy Geosciences Division, Lawrence Berkeley National Laboratory, Berkeley, USA

ARTICLE INFO

Article history:
Received 1 June 2019
Received in revised form
13 December 2019
Accepted 31 December 2019
Available online 19 May 2020

Keywords:
Fracture
Stress
Aperture
Connectivity
Permeability

ABSTRACT

In this study, the combined effects of geometrical distribution and geomechanical deformation of fracture networks on fluid flow through fractured geological media are investigated numerically. We consider a finite-sized model domain in which the geometry of fracture systems follows a power-law length scaling. The geomechanical response of the fractured rock is simulated using a hybrid finite-discrete element model, which can capture the deformation of intact rocks, the interaction of matrix blocks, the displacement of discrete fractures and the propagation of new cracks. Under far-field stress loading, the locally variable stress distribution in the fractured rock leads to a stress-dependent variable aperture field controlled by compression-induced closure and shear-induced dilatancy of rough fractures. The equivalent permeability of the deformed fractured rock is calculated by solving for the fracture-matrix flow considering the cubic relationship between fracture aperture and flow rate at each local fracture segment. We report that the geometrical connectivity of fracture networks plays a critical role in the hydromechanical processes in fractured rocks. A well-connected fracture system under a high stress ratio condition exhibits intense frictional sliding and large fracture dilation/opening, leading to greater rock mass permeability. However, a disconnected fracture network accommodates much less fracture shearing and opening, and has much lower bulk permeability. We further propose an analytical solution for the relationship between the equivalent permeability of fractured rocks and the connectivity metric (i.e. percolation parameter) of fracture networks, which yields an excellent match to the numerical results. We infer that fluid flow through a well-connected system is governed by traversing channels (forming an "in parallel" architecture) and thus equivalent permeability is sensitive to stress loading (due to stress-dependent fracture permeability), whilst fluid flow through a disconnected system is more ruled by matrix (linking isolated clusters "in series") and has much less stress dependency.
© 2020 Institute of Rock and Soil Mechanics, Chinese Academy of Sciences. Production and hosting by Elsevier B.V. This is an open access article under the CC BY-NC-ND license (http://creativecommons.org/licenses/by-nc-nd/4.0/).

1. Introduction

Natural fractures often form complex networks in the Earth's crust and serve as important pathways for fluid migration in subsurface geological media (Tsang and Neretnieks, 1998). The geometrical distribution of these natural discontinuities controls the global connectivity of passage systems (Bonnet et al., 2001), while the geomechanical deformation of contacting fracture surfaces under in situ stress loading dominates the local transmissivity of individual channels (Rutqvist and Stephansson, 2003). Thus, the understanding of fluid flow in fractured geological formations requires a comprehensive characterisation of both the geometrical properties and geomechanical responses of the embedded natural fracture networks (Zimmerman and Main, 2004; Lei et al., 2017a).

Fracture patterns are spatially organised by mechanical interactions that emerge during their growth (Pollard and Aydin, 1988), which creates a hierarchical geometry exhibiting long-range correlations from macroscale frameworks to microscale

* Corresponding author.
E-mail address: xiaoguang.wang@umontpellier.fr (X. Wang).
Peer review under responsibility of Institute of Rock and Soil Mechanics, Chinese Academy of Sciences.

https://doi.org/10.1016/j.jrmge.2019.12.014
1674-7755 © 2020 Institute of Rock and Soil Mechanics, Chinese Academy of Sciences. Production and hosting by Elsevier B.V. This is an open access article under the CC BY-NC-ND license (http://creativecommons.org/licenses/by-nc-nd/4.0/).

fabrics (Barton, 1995). Such geometrical complexities are often depicted in terms of fracture size, density, orientation and aperture as well as connectivity (Bonnet et al., 2001). By mimicking the distributions of these properties following statistical/stochastic principles, synthetic discrete fracture networks are often generated to represent natural discontinuity systems (Dershowitz and Einstein, 1988), based on which subsurface fluid flow properties and processes can be studied (Long et al., 1982; Long and Billaux, 1987; Berkowitz, 2002; Min et al., 2004a; Wang et al., 2017). Many theoretical and numerical investigations have suggested that the hydraulic connectivity of fracture networks, embedded in impervious or low permeability rocks, crucially controls the bulk permeability and fluid movements (Hestir and Long, 1990; Berkowitz, 1995; Bour and Davy, 1997, 1998; Renshaw, 1999; de Dreuzy et al., 2001a; Liu et al., 2016). In addition, the non-trivial impacts of variable fracture apertures on fluid flow have been analysed via making ad hoc hypotheses for their statistics (de Dreuzy et al., 2001b; Baghbanan and Jing, 2007; Klimczak et al., 2010), whereas the sensitive nature of fracture openings in response to geomechanical processes was often omitted.

The presence of natural fractures can induce strong local stress perturbations in geological media subjected to far-field stress loading (Lei and Gao, 2018, 2019). The locally varying stress distribution leads to variable normal and/or shear forces across fracture walls of widely-ranging sizes and orientations, producing a variety of fracture responses such as closure, sliding, dilatancy and propagation (Min et al., 2004b; Latham et al., 2013; Lei et al., 2016). Since the conductivity of fractures is critically dependent on the third power of fracture apertures (Witherspoon et al., 1980), these geomechanical processes accommodated in fractures can considerably affect the bulk hydrological properties of fractured porous media, especially if the matrix is much less permeable than fractures (Rutqvist, 2015). Overburden-induced confinement of fractured rocks tends to reduce fracture apertures and suppress fluid flow (Bandis et al., 1983; Barton et al., 1985), leading to the general trend of decreased rock mass permeability with increased formation depth (Rutqvist and Stephansson, 2003). On the other hand, large differential stresses imposed within the critically stressed crust can promote sliding and dilatancy along rough fractures, resulting in flow localisation and permeability enhancement, as revealed by many numerical results (Sanderson and Zhang, 1999; Min et al., 2004b; Baghbanan and Jing, 2008; Latham et al., 2013; Lei et al., 2014, 2015; 2017b; Lang et al., 2018; Kang et al., 2019; Jiang et al., 2019). However, these previous modelling studies mainly focused on sophisticated geomechanical processes while placing little emphasis on the role of geometrical properties, and therefore the analysis was usually only based on a specifically selected or generated fracture network.

In reviewing the extensive studies in the literature about hydromechanical processes in fractured rocks (Rutqvist and Stephansson, 2003; Lei et al., 2017a), we identify that little effort has been devoted to understanding the mutual effects of fracture network geometry and geomechanics on subsurface fluid flow as well as distinguishing the relative importance of each process. Thus, in this paper, we aim to use the state-of-the-art numerical simulation to gain insights into how these two aspects interactively affect the hydrological properties of fractured rocks. The remainder of the paper is organised as follows. Section 2 describes a set of approaches for modelling fracture network geometry, solid skeleton deformation, rough fracture behaviour and fluid flow field. Section 3 presents the model setup and boundary conditions for numerical experiments, with the numerical results further elucidated in Section 4. Finally, a discussion is given and conclusions are drawn in Section 5.

2. Methodology

2.1. Fracture network model

Natural fracture systems often exhibit a broad range of fracture lengths that can be described by a power-law statistical model with a density function given as (Bonnet et al., 2001; Lei and Wang, 2016):

$$n(l,L) = \alpha L^D l^{-a} \qquad (l \in [l_{\min}, l_{\max}]) \tag{1}$$

where l is the fracture length, L is the domain size, a is the power-law length exponent, D is the fractal dimension, and α is the density term. The only intrinsic characteristic length scales in this model are the smallest and largest fracture lengths, i.e. $l_{\min}$ and $l_{\max}$, respectively. In numerical simulations, L is the scale of the modelling domain, which usually meets $l_{\min} << L << l_{\max}$. Extensive outcrop data suggest that D value generally varies between 1.5 and 2, and a falls between 1.5 and 3.5 (Bonnet et al., 2001).

The fracture intensity γ (also known as the mass density), i.e. total length of fractures per unit area, is related to the first moment of the density distribution of fracture lengths as

$$\gamma = \frac{1}{L^2}\int_{A_L} n(l,L) l' \mathrm{d}l \tag{2}$$

where l' denotes the fracture length included in the domain of an area $A_L = L^2$. The percolation parameter p as a connectivity metric of fracture networks is given by (Bour and Davy, 1997):

$$p = \frac{1}{L^2}\int_{A_L} n(l,L) l'^2 \mathrm{d}l \tag{3}$$

The higher the p is, the more connected the system is. The network is statistically connected if p is greater than the percolation threshold p_c, whose value is in general scale-invariant and within a narrow range between 5 and 7, i.e. $p_c = 6 \pm 1$ for two-dimensional (2D) random fracture networks with $D = 2$ (Bour and Davy, 1997).

2.2. Geomechanical model

The geomechanical model is based on a hybrid finite-discrete element method (FDEM) (Munjiza, 2004), which can realistically capture the stress/strain evolution in intact rocks, interaction between matrix blocks, deformation of pre-existing fractures, and propagation of new cracks (Lei et al., 2017a). The FDEM model represents 2D fractured rock using an unstructured, fully-discontinuous mesh of three-node triangular finite elements, which are linked by four-node joint elements (see Fig. 1). There are two types of joint elements: unbroken joint elements inside the matrix and broken joint elements along fractures (Lei et al., 2016). The joint elements (either broken or unbroken) are created and embedded between the edges of triangular element pairs before the numerical simulation and no remeshing is performed during later computation.

The motion of finite elements is governed by the forces acting on the elemental nodes (Munjiza, 2004):

$$\boldsymbol{M}\ddot{\boldsymbol{x}} + \boldsymbol{f}_{\mathrm{int}} = \boldsymbol{f}_{\mathrm{ext}} \tag{4}$$

where $\boldsymbol{M}$ is the lumped nodal mass matrix; $\boldsymbol{x}$ is the vector of nodal displacements; $\boldsymbol{f}_{\mathrm{int}}$ is the internal nodal force induced by the deformation of triangular elements; and $\boldsymbol{f}_{\mathrm{ext}}$ is the external nodal force including external load $\boldsymbol{f}_{\mathrm{l}}$ contributed by boundary conditions

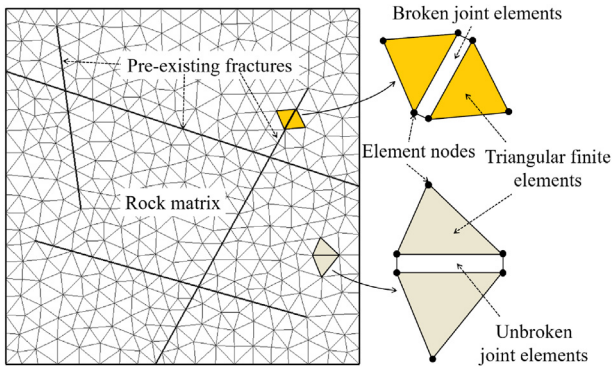

Fig. 1. Representation of a 2D fractured rock using an unstructured, fully-discontinuous mesh of three-node triangular finite elements linked by four-node joint elements.

and body forces, cohesive bonding force $\boldsymbol{f}_b$ caused by the deformation of unbroken joint elements, and contact force $\boldsymbol{f}_c$ generated by the contact interaction via broken joint elements. The deformation of intact rocks is captured by linear-elastic constant-strain finite elements with the continuity constrained by the bonding forces of unbroken joint elements (Munjiza et al., 1999). The interaction of discrete matrix bodies is calculated based on the penetration of finite elements via broken joint elements (Munjiza and Andrews, 2000). The elasto-plastic fracturing in formation rocks is modelled by a smeared crack (i.e. cohesive zone) method that can capture the nonlinear stress-strain behaviour of the plastic zone ahead of each fracture tip (Munjiza et al., 1999). The equations of motion of the FDEM model are solved through an explicit time integration scheme based on the forward Euler method.

2.3. Fracture constitutive model

The closure of rock fractures under compression is calculated based on a hyperbolic relation (Bandis et al., 1983) (Fig. 2a):

$$v_n = \frac{\sigma_n v_m}{k_{n0} v_m + \sigma_n} \tag{5}$$

where v_n is the normal closure, σ_n is the effective normal compressive stress derived from the Cauchy stress tensor of adjacent finite elements, k_{n0} is the initial normal stiffness, and v_m is the maximum allowable closure.

The shear deformation of rock fractures is calculated based on an elasto-plastic constitutive model with strain-softening (Goodman, 1976; Saeb and Amadei, 1992) (Fig. 2b). In the elastic phase, the shear stress τ increases linearly with the shear displacement u, and the slope of the stress-displacement curve is given by the shear stiffness k_s. During this stage, the opposing fracture walls ride over each other's asperities, resulting in dilational displacement in the normal direction (Fig. 2c). The peak shear stress τ_p is eventually reached when the displacement arrives at the peak shear displacement u_p, beyond which the asperities begin to shear off and irreversible damage on the surfaces starts to occur. If the fracture continues to slide, the shear stress decreases linearly to the residual shear stress τ_r, during which the asperities are crushed and sheared off and the dilation continues. Finally, when the displacement exceeds the residual displacement u_r, the shear stress remains constant (i.e. $\tau = \tau_r$), and no further dilation develops. The dependency of the shear behaviour of fractures on normal stress loading is described using a constant displacement model characterised with fixed u_p and u_r values (Goodman, 1976).

The peak shear stress τ_p is given by (Ladanyi and Archambault, 1969; Saeb and Amadei, 1992):

$$\tau_p = \sigma_n \tan(\phi_b + \phi_i)(1 - a_s) + a_s c \tag{6}$$

where a_s is the proportion of total fracture area sheared through asperities; ϕ_i is the dilation angle; c is the shear strength of the asperity (i.e. cohesion of the intact rock); and ϕ_b is the basic friction angle which, for unweathered conditions, can be substituted using the residual friction angle ϕ_r (Barton and Choubey, 1977). If σ_n does not exceed the uniaxial compressive strength of the intact rock σ_u, the values of a_s and ϕ_i are respectively given as (Ladanyi and Archambault, 1969):

$$a_s = 1 - \left(1 - \frac{\sigma_n}{\sigma_u}\right)^{m_1} \tag{7}$$

$$\tan\phi_i = \begin{cases} \left(1 - \frac{\sigma_n}{\sigma_u}\right)^{m_2} \tan\phi_{i0} & (u \le u_r) \\ 0 & (u > u_r) \end{cases} \tag{8}$$

where ϕ_{i0} is the initial dilation angle when $\sigma_n = 0$; and m_1 and m_2 are the empirical parameters with suggested values of 1.5 and 4, respectively. The residual shear stress τ_r is given as (Barton and Choubey, 1977):

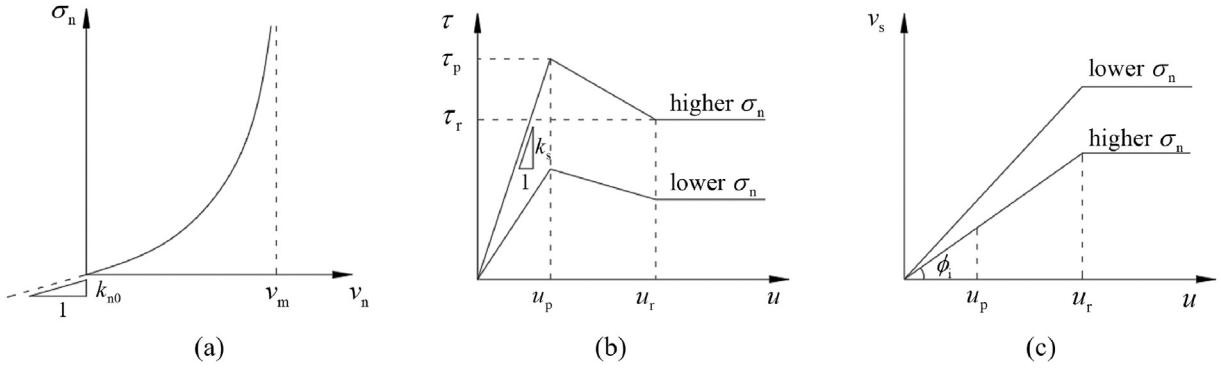

Fig. 2. Fracture deformation model: (a) Normal closure v_n as a function of effective normal stress σ_n; (b) Shear stress τ as a function of shear displacement u; and (c) Dilational displacement v_s as a function of shear displacement u.

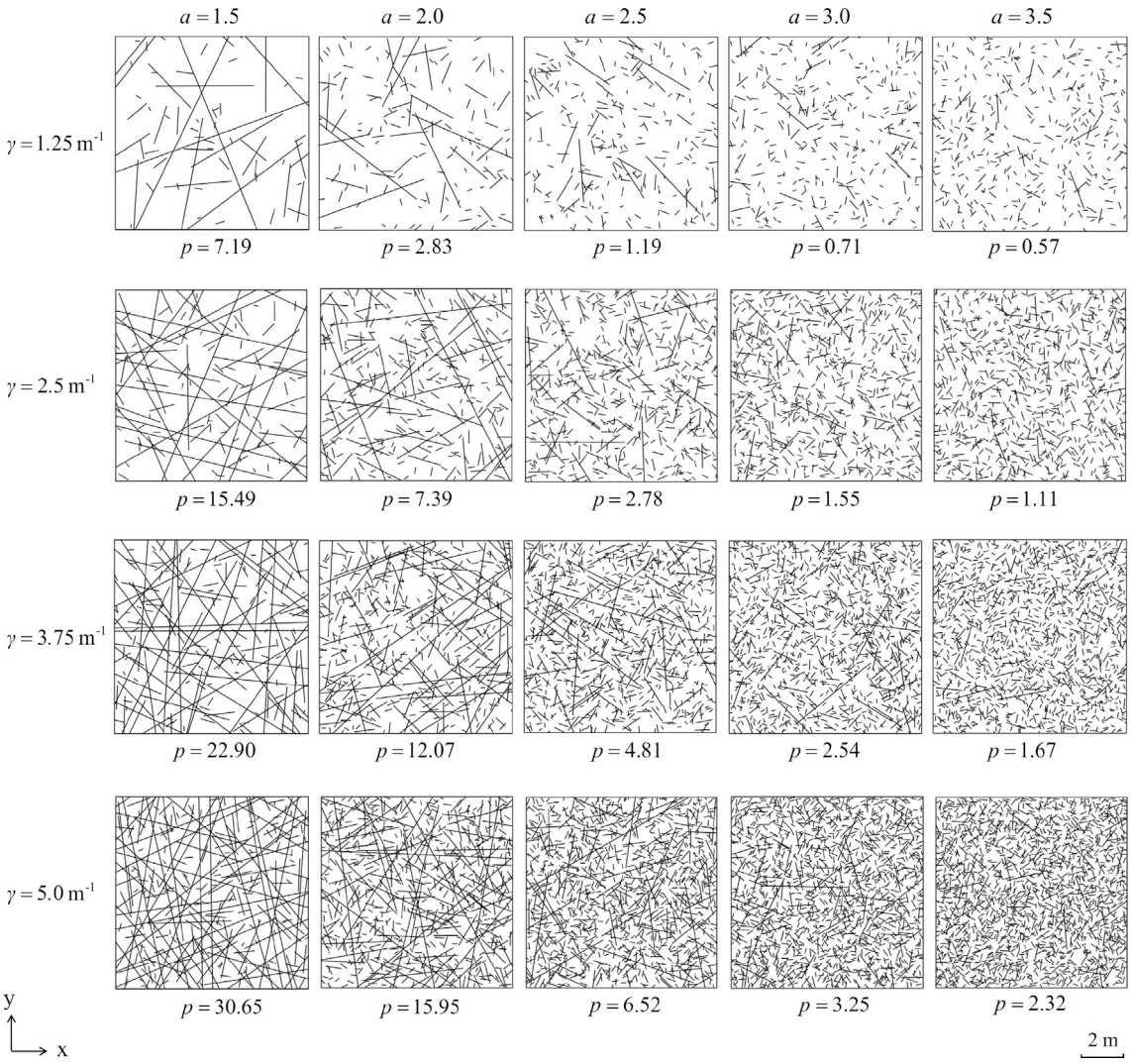

Fig. 3. The geometry of generated fracture networks (domain size $L = 10$ m) associated with various power-law length exponent a and mean fracture intensity γ. The percolation parameter p of each network is calculated for each network. Note that ten realisations are created for each combination of a and γ, but only one realisation for each case is shown here.

$$\tau_r = \sigma_n \tan \phi_r \tag{9}$$

The dilational displacement v_s under a constant normal stress condition is related to the shear displacement in an incremental form as (Saeb and Amadei, 1992):

$$dv_s = -\tan \phi_i du \tag{10}$$

The fracture aperture h under coupled normal and shear loadings is thus given by (Lei et al., 2016):

$$h = \begin{cases} h_0 + w & (\sigma_n < 0) \\ h_0 - v_n - v_s & (\sigma_n \geq 0) \end{cases} \tag{11}$$

where h_0 is the initial aperture, and w is the separation of opposing fracture walls if the fracture is under tension. The local fracture permeability is then calculated based on the cubic law as $h^2/12$ (Witherspoon et al., 1980).

2.4. Fluid flow model

Fluid flow through fractured rock with multiple intersecting fractures and permeable matrix is further solved. Single-phase steady-state flow of incompressible fluid with constant viscosity through porous media, in absence of sources and sinks, is governed by the continuity equation and Darcy's law, which is reduced to a Laplace equation as

$$\nabla \cdot (k \nabla P) = 0 \tag{12}$$

where k is the intrinsic and isotropic permeability of the porous media with local variability permitted, and P is the fluid pressure calculated at the nodes of unstructured finite element grids. The element-wise constant barycentric velocity is resolved based on the pressure gradient vector field by applying Darcy's law given by

$$\boldsymbol{u}^e = -\frac{k^e}{\mu} \nabla P^e \tag{13}$$

where $\boldsymbol{u}^e$ is the vector field of element-wise constant velocities; P^e is the local element pressure field; μ is the dynamic fluid viscosity; and k^e is the local permeability of a matrix volumetric element with an assumed constant value or a lower dimensional fracture element having a stress-dependent value, i.e. $h^2/12$. By applying a prescribed macroscopic pressure differential on each pair of opposite

boundary surfaces with no-flow conditions on the remaining ones parallel to the flow direction, the pressure diffusion is computed for all the fracture and matrix elements of the entire domain. The equivalent permeability of the fractured media is then derived using element volume weighted averaging of pressure gradients and fluxes:

$$\frac{1}{V}\sum_{\mathrm{e}}\int_{V^{\mathrm{e}}} u_j^{\mathrm{e}}\,\mathrm{d}V^{\mathrm{e}} = \frac{k_{ij}}{\mu}\frac{1}{V}\sum_{\mathrm{e}}\int_{V^{\mathrm{e}}}\frac{\partial P^{\mathrm{e}}}{\partial x_i}\mathrm{d}V^{\mathrm{e}} \tag{14}$$

where u_j^{e} is the element-wise barycentric velocity in the j direction, $\partial P^{\mathrm{e}}/\partial x_i$ is the element pressure gradient along x_i, and k_{ij} is the component of the permeability tensor.

3. Model setup

In this study, we generate a series of 2D synthetic fracture networks in a square domain of size $L = 10$ m (Fig. 3). The location and orientation of fractures are assumed purely random, i.e. nominally homogeneous (i.e. $D = 2$) and isotropic. The fracture lengths follow the power-law scaling, with the bounds given by $l_{\min} = L/50 = 0.2$ m and $l_{\max} = 50L = 500$ m. We explore five different length exponent cases, i.e. $a = 1.5$, 2, 2.5, 3 and 3.5, and four mean fracture intensity scenarios, i.e. $\gamma = 1.25$ m^{-1}, 2.5 m^{-1}, 3.75 m^{-1} and 5 m^{-1}. For each combination of a and γ, ten realizations are generated, with their p values also derived. As shown in Fig. 3, when $a \leq 2$, the system is dominated by domain-sized, very large fractures; when $a \geq 3$, the system mainly consists of small fractures; when $2 < a < 3$, both large and small fractures tend to be important. It can also be noted that an increased a leads to a reduction in the geometrical connectivity, i.e. decreased p. The fracture networks generated here cover the scenarios of below ($p < 5$), around ($5 \leq p \leq 7$) and beyond ($p > 7$) the percolation threshold, representing the disconnected, transitional and connected regimes, respectively.

The assumed material properties of the fractured rocks are given in Table 1, based on the typical ranges for crystalline rocks in the literature (Lama and Vutukuri, 1978; Bandis et al., 1983; Zoback, 2007). The energy release rates are estimated based on empirical correlations (Zhang, 2002; Jin et al., 2011). The problem domain containing distributed fractures is discretised using an unstructured mesh with an average element size of 0.05 m. The penalty term and damping coefficient are chosen to be 500 GPa and 2×10^5 kg/(m s), respectively, based on the recommendations in the literature (Munjiza, 2004; Mahabadi, 2012). Effective far-field stresses are loaded orthogonally to the model (Fig. 4a), and we consider three different scenarios: (i) $S_x = 5$ MPa, $S_y = 5$ MPa, (ii) $S_x = 10$ MPa, $S_y = 5$ MPa, and (iii) $S_x = 15$ MPa, $S_y = 5$ MPa, such that the effective far-field stress ratio S_x/S_y is 1, 2, and 3, respectively. Single-phase steady-state fluid flow through the deformed fractured rock having a stress-dependent aperture field is further modelled by imposing the classical permeameter boundary condition (Fig. 4b): two opposite boundary surfaces of the model domain have a fixed pressure drop (i.e. 10 kPa), while the two orthogonal boundaries parallel to the flow direction are impervious. Matrix permeability k_{m} is assumed to be 1×10^{-18} m^2, which gives a high fracture-matrix permeability contrast so that the flow is predominated by fractures (Matthäi and Belayneh, 2004).

Table 1
Material properties of the fractured rocks (Lama and Vutukuri, 1978; Bandis et al., 1983; Zoback, 2007).

Material	Property	Unit	Value
Intact rocks	Density, ρ	kg/m^3	2700
	Young's modulus, E	GPa	50
	Poisson's ratio, ν		0.25
	Internal friction angle, ϕ_{int}	°	45
	Tensile strength, f_{t}	MPa	20
	Cohesion, c	MPa	40
	Uniaxial compressive strength, σ_{u}	MPa	193.1
	Mode I energy release rate, G_{I}	J/m^2	158.4
	Mode II energy release rate, G_{II}	J/m^2	198
	Matrix permeability, k_{m}	m^2	1×10^{-18}
Fractures	Initial aperture, h_0	mm	0.1
	Maximum allowable closure, v_{m}	mm	0.09
	Initial normal stiffness, k_{n0}	GPa/m	50
	Residual friction angle, ϕ_{r}	°	31
	Peak shear displacement, u_{p}	mm	1
	Residual shear displacement, u_{r}	mm	3
	Initial dilation angle, ϕ_{i0}	°	10

The constructed models are numerically solved using the methods described in Section 2. It is worth pointing out that the advantages of our approaches, compared to many other previous studies/methods (e.g. Min et al., 2004b; Baghbanan and Jing, 2008), include simulation of crack growth in intact rocks and consideration of fluid flow in permeable matrix. Newly-formed cracks under stress loadings may cause coalescence of initially isolated fractures/clusters, capture what is essential for modelling the hydromechanical behaviour of fracture networks around the percolation threshold. The consideration of fluid flow in permeable matrix is important for studying fracture networks below the percolation threshold, where fluid cannot migrate purely through fractures.

4. Results

4.1. Geomechanical responses

We analyse the geomechanical responses of the fractured rocks associated with a range of combinations of length exponent a and fracture intensity γ values under different far-field stress conditions. The numerical results for the case of $\gamma = 2.5$ m^{-1} are shown in Fig. 5, while the results for other cases of $\gamma = 1.25$ m^{-1}, 3.75 m^{-1} and 5 m^{-1} are given in Figs. A1, A2 and A3, respectively (see Appendix). Below, we take Fig. 5 as an example to elucidate the key geomechanical processes in fracture networks and similar phenomena or trends can also be observed in Figs. A1-A3.

Fig. 5a shows the distributions of local maximum principal stresses in the fractured rocks with $\gamma = 2.5$ m^{-1} and different a values. When the far-field stress condition is isotropic, i.e. $S_x = S_y = 5$ MPa, the local stress distribution is very uniform. As the far-field stress ratio S_x/S_y increases, stress fluctuations emerge in the system, especially when S_x/S_y reaches 3. It can be seen that the high stress bands tend to align with the orientation of the applied far-field maximum principal stress but are significantly distorted due to the presence of pre-existing discontinuities. It seems that with the increase of a (i.e. the system is more dominated by small fractures), the stress patterns become less heterogeneous.

Fig. 5b shows the distribution of shear displacements in the stressed fracture networks. When the far-field stresses are isotropically loaded, almost no shear displacement occurs in the system, irrespective of the geometrical distribution of fracture populations. As S_x/S_y value increases to 2, noticeable shear displacements are accommodated along some of the large fractures that are oriented to favour frictional sliding. When S_x/S_y equals 3, preferentially-oriented, large fractures in the networks of $a \leq 2$ are highly reactivated for shear slip, whereas the remaining relatively smaller fractures experience much less shearing. In the fracture networks of $a \geq 3$, which are dominated by small cracks, frictional sliding is strongly suppressed, although some intermediate fractures might exhibit slight shear. In the fracture networks of $2 < a <$

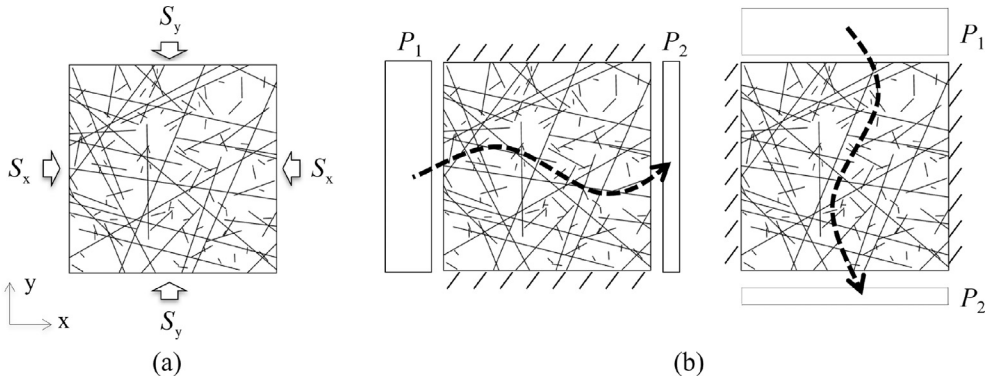

Fig. 4. Model setup for (a) geomechanical simulation and (b) fluid flow simulation. S_x and S_y denote the effective far-field stresses loaded orthogonally to the model. P_1 and P_2 gives the macroscopic pressure difference imposed across the domain.

3, which consist of both large and small fractures, some large structures tend to be moderately sheared while the small cracks are mostly restrained for any sliding.

In Fig. 5c, we show the distribution of fracture apertures in the fractured networks under the combined effects of compression-induced closure and shear-induced dilatancy. When $S_x/S_y = 1$, all fractures are evenly compressed and exhibit an aperture much lower than the initial value, i.e. 0.1 mm. As S_x/S_y increases to 2, some traversing fractures in the networks of $a \leq 2$ exhibit large apertures because of shear-induced dilation along these dominant structures that are preferentially-oriented for sliding. However, some small fractures sub-parallel to S_y seem to be more closed due to the increased S_x, compared to those under isotropic compression. When S_x/S_y reaches 3, in the networks of $a \leq 2$, drastic enlargement of fracture apertures occurs along those highly-sheared large discontinuities due to the dilational behaviour of dislocated rough fracture walls. However, the fracture networks of $a \geq 3$ exhibit much less fracture opening, although some intermediate fractures still experience small amount of shear-induced aperture increase. In the fracture networks of $2 < a < 3$, large fractures are associated with shear-induced wider apertures while small fractures only exhibit closure manner.

We further calculate the length-averaged mean shear displacement $\overline{u}$ and mean fracture aperture $\overline{h}$ of each fracture network and examine their variation as a function of various geometrical properties, i.e. a, γ and p, under different far-field stress loading conditions (Fig. 6). When $S_x/S_y = 1$, $\overline{u}$ is almost zero and insensitive to the change of a, γ or p (Fig. 6a, c and e), while $\overline{h}$ is also independent of a, γ or p (Fig. 6b, d and f) and exhibits a value much lower than the initial aperture of $h_0 = 0.1$ mm. As S_x/S_y increases, more frictional sliding is accommodated in the system due to the enhanced differential stress load. When $S_x/S_y > 1$, $\overline{u}$ increases significantly with the decrease of a (Fig. 6a) or increase of p (Fig. 6e), suggesting that the fracture networks associated with larger fractures or better connectivity tend to accommodate more frictional sliding driven by deviatoric stress loading. Similarly, $\overline{h}$ increases considerably with the decrease of a (Fig. 6b) or increase of p (Fig. 6f), as a result of fracture dislocation and dilation under differential stresses. Especially, in the well-connected fracture systems ($p > p_c$) subjected to high stress ratio loading ($S_x/S_y = 3$), the resulting aperture $\overline{h}$ can become even larger than the initial aperture h_0 (Fig. 6f) due to the combined effects of geometrical properties and geomechanical processes. In addition, it is noticed that both $\overline{u}$ and $\overline{h}$ seem to be almost uncorrelated with γ (Fig. 6c and d). A further interpretation and discussion can be found in in Section 5.

4.2. Hydrological properties

We derive the hydrological properties of the deformed fractured porous rocks from the single-phase steady-state flow simulation. Fig. 7 shows the distribution of local fluid flow velocity in different fracture systems subjected to the far-field stress condition of $S_x = 15$ MPa and $S_y = 5$ MPa and with the macroscopic pressure drop imposed along the x- (Fig. 7a) or y-direction (Fig. 7b). The numerical results for other far-field stress conditions are given in the Appendix (see Figs. A4 and A5). In the networks that are below the percolation threshold ($p < p_c$), the flow velocity is extremely low, since fluid has to migrate via intact rocks of low permeability that bridge disconnected fractures. On the other hand, the well-connected networks ($p > p_c$) accommodate significantly high flow velocities along through-going discontinuities, whereas the "background" small cracks with "dead-ends" provide much lower velocities. If the system is around the percolation threshold ($p \approx p_c$), e.g. the fracture network of $a = 2.5$ and $\gamma = 5$ m^{-1}, only one or two globally-connected pathways exist(s) for fast fluid migration, whereas other locally-connected clusters permit much slower flow. In such a critically-connected system ($p \approx p_c$), multiple clusters bounded by large fractures seem to exhibit distinct regimes of velocity magnitudes, implying the dominant roles of large discontinuities on the flow field.

Fig. 8 shows the variation of the equivalent permeability k_{eq} (either k_{xx} or k_{yy}) of the fractured rocks as a function of various geometrical properties, i.e. a, γ and p, under different far-field stress loading conditions. It can be seen that, with the increase of a, the permeability generally decreases (Fig. 8a and b), because the system becomes more controlled by small fractures, which geometrically have less probability to form connected pathways (i.e. poorer connectivity) and geomechanically have less opportunity to experience frictional sliding (i.e. smaller dilation). Due to these geometrical and geomechanical effects, k_{eq} is very sensitive to stress loading if a is small (e.g. $a = 1.5$), whilst almost independent of the far-field stress state if a is large (e.g. $a = 3.5$). The rock mass permeability seems to increase with γ, but the trend exhibits large uncertainties (Fig. 8c and d). On the contrary, the correlation between k_{eq} and p is very significant (Fig. 8e and f). If the fracture network is disconnected ($p < p_c$), k_{eq} is very small, due to the flow-restriction caused by low-permeability rocks that isolate discrete fractures or fracture clusters from connecting with each other across the entire domain. The stress-dependent fracture deformational behaviour therefore exerts very minor impacts on k_{eq}. However, as the fracture network becomes gradually connected ($p \geq p_c$), an abrupt increase in k_{eq}

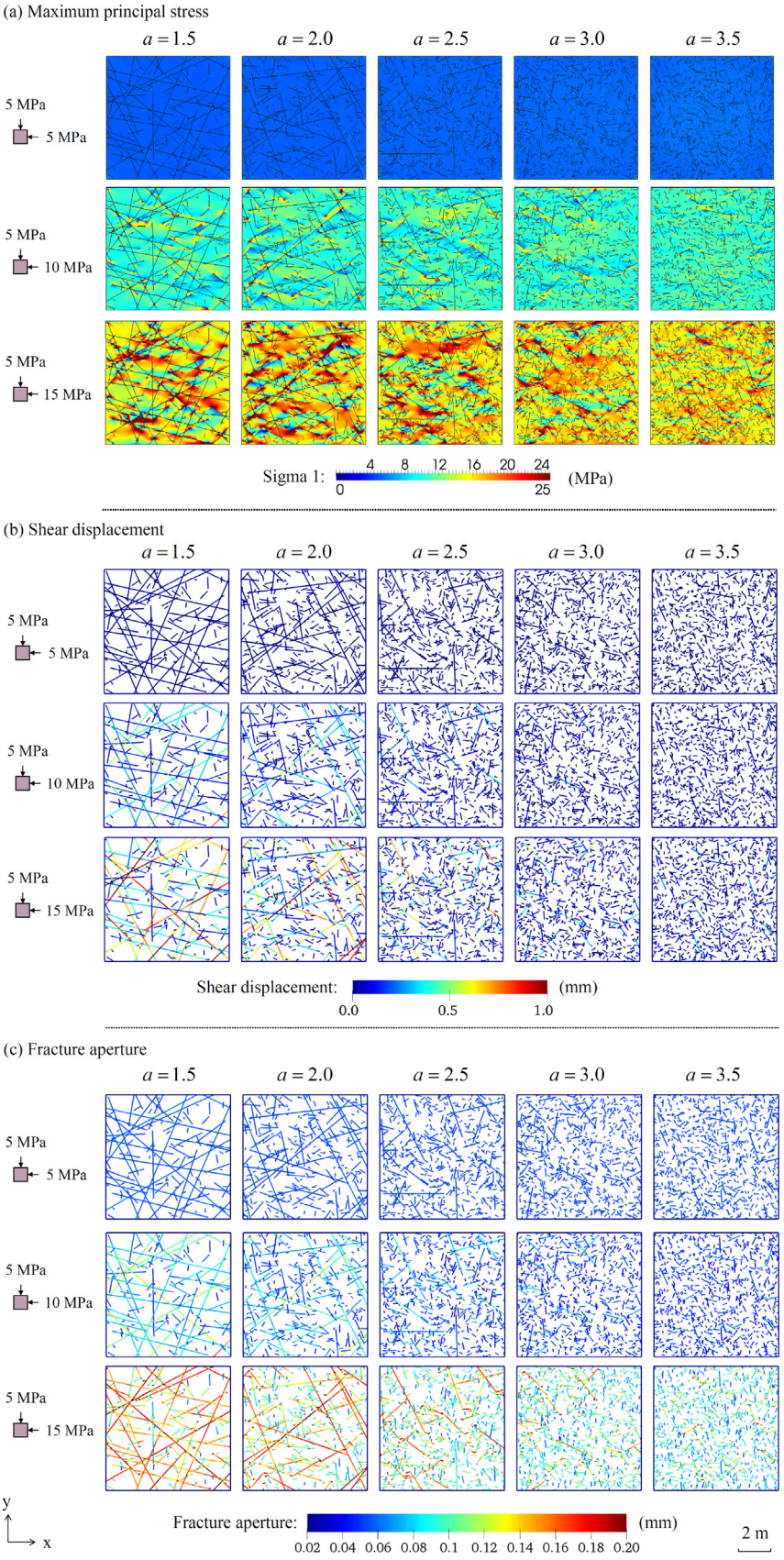

Fig. 5. Distributions of (a) local maximum principal stress, (b) shear displacement, and (c) fracture aperture in the fractured rocks with a fixed fracture intensity $\gamma = 2.5\ m^{-1}$ and various length exponents a = 1.5, 2, 2.5, 3 and 3.5, under different far-field stress conditions.

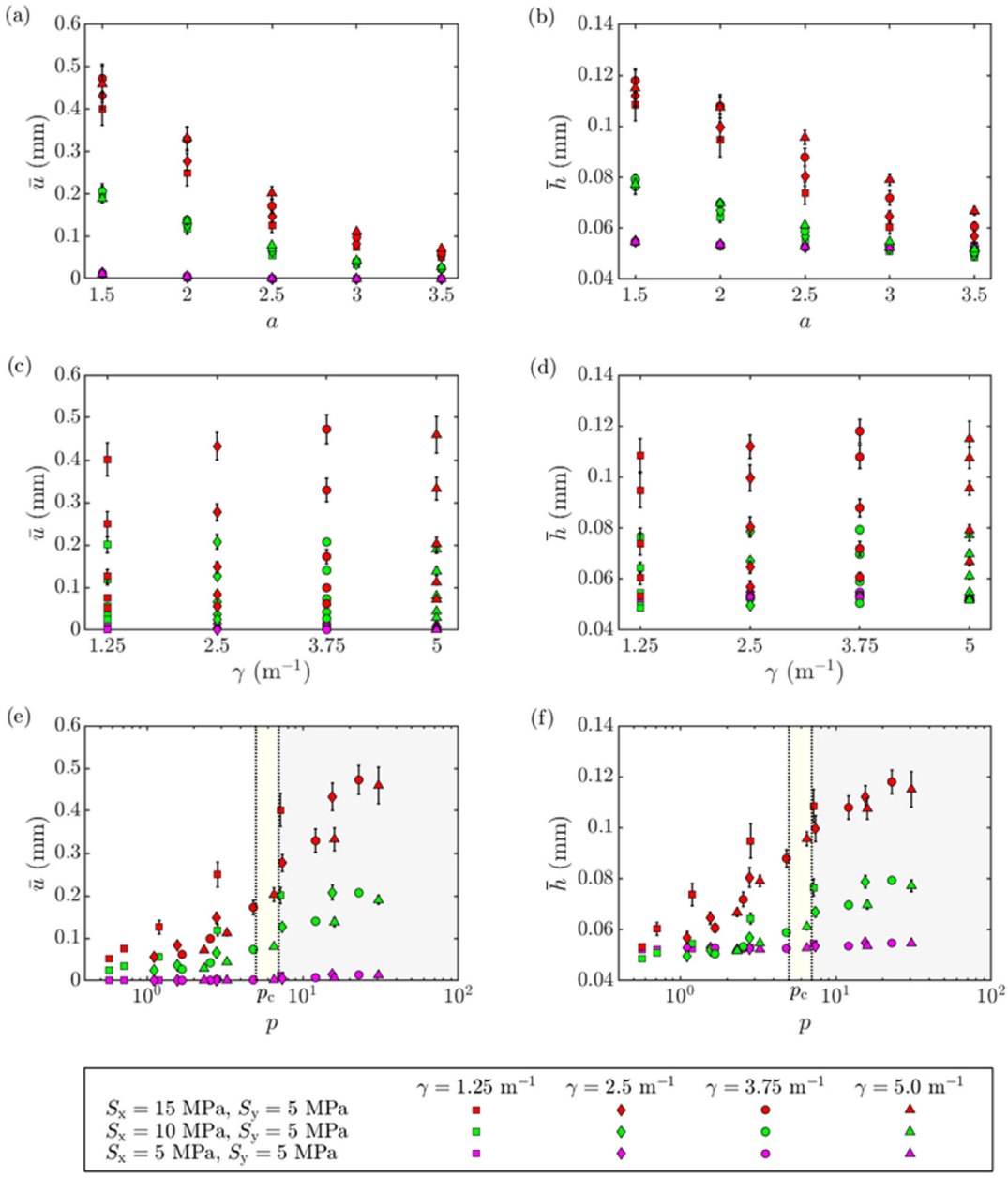

Fig. 6. The mean shear displacement $\bar{u}$ (left panel) and mean fracture aperture $\bar{h}$ (right panel) of the fractured network as a function of different geometrical properties, i.e. (a, b) length exponent a, (c, d) fracture intensity γ, and (e, f) percolation parameter p, under different far-field stress conditions. The error bars denote ±1 standard deviation of the ten realisations. The zone bounded by dotted lines in (e, f) corresponds to the percolation threshold $p_c = 6 \pm 1$.

occurs, since the interconnected backbones of high transmissivity (compared to matrix rocks) start to play the controlling role in carrying fluid migration, which further leads to the variation of k_{eq} in response to the change of boundary stress loading as a result of the important geomechanical processes illustrated in Fig. 5, A1 and A2.

We further derive analytical solutions to investigate the relationship between k_{eq} and p. We characterise their correlation based on the three different regimes: disconnected ($p < p_c$), transitional ($p \approx p_c$) and connected ($p > p_c$). If the system is connected, fluid flow is controlled by interconnected fractures that form the major pathways and the equivalent permeability of the percolated fracture system may be predicted using the percolation theory (Stauffer and Aharony, 1985):

$$k_{eq} = k_c(p - p_c)^{\beta} \quad (p > p_c) \tag{15}$$

where β is a universal exponent and equals 1.1 for 2D systems (Hestir and Long, 1990; Berkowitz and Balberg, 1993), and k_c is the equivalent permeability when $p-p_c$ equals unity. k_c is expected to be controlled by single fracture permeability, because the system is close to the percolation threshold and the connectivity is ruled by a limited number of "red links" (Davy et al., 2006). Thus, we postulate that $k_c = \lambda h^3/(12L)$, where λ is the number of red links. We take $p_c = 6$, $L = 10$ m and $\lambda = 3$ (p approaches p_c from above). Then, for the three different stress cases of $S_x/S_y = 1$, 2 and 3, we choose $h = 0.05$ mm, 0.07 mm and 0.11 mm (Fig. 6), respectively, and thus derive k_0 to be 3×10^{-15} m^2, 8.6×10^{-15} m^2 and 2.5×10^{-14} m^2, respectively. The analytical solutions based on these parameters

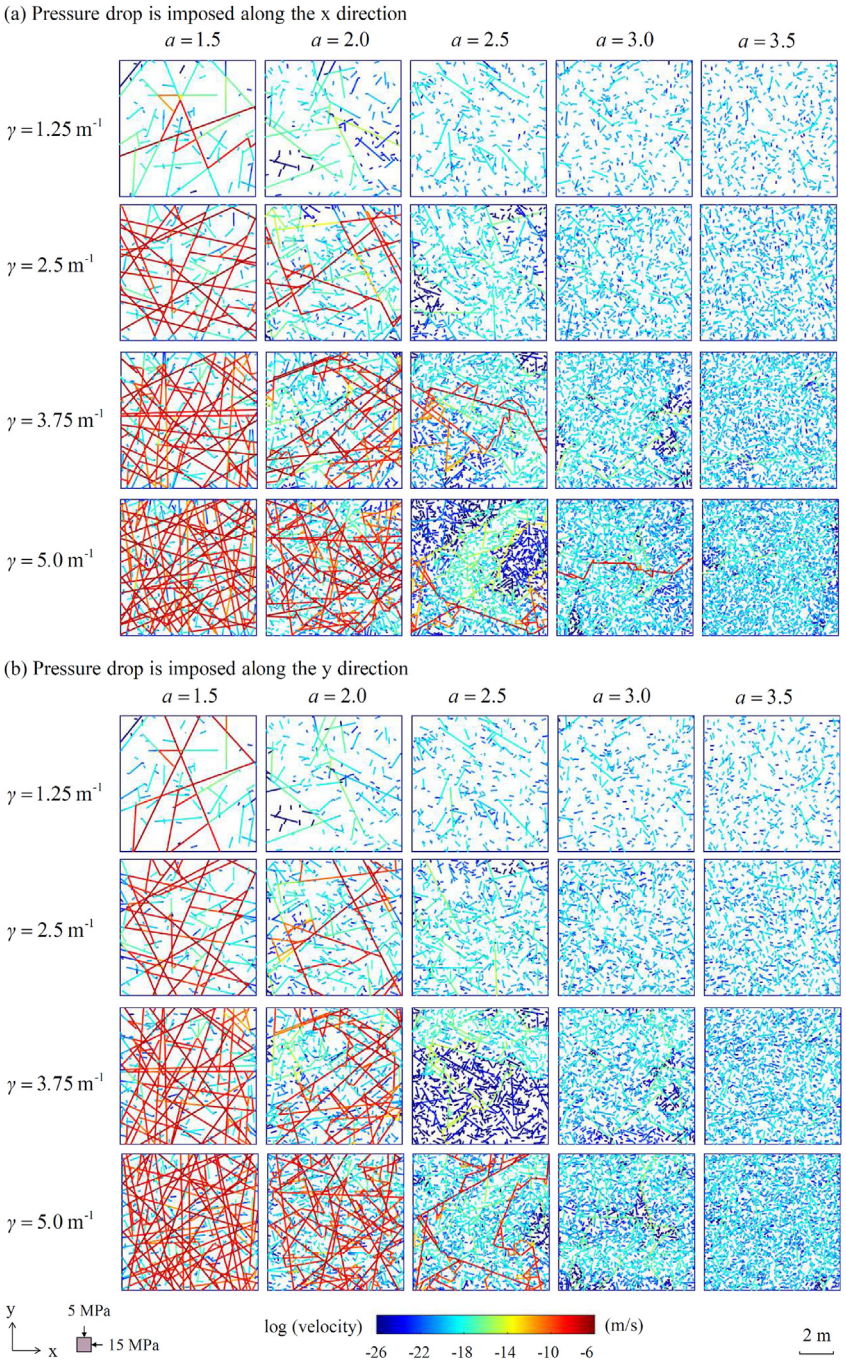

Fig. 7. Distribution of flow velocity in the fracture networks associated with various length exponents a and fracture intensities γ under the far-field stress condition of $S_x = 15$ MPa and $S_y = 5$ MPa. The macroscopic pressure drop is imposed along either the (a) x or (b) y direction.

show an excellent match to the numerical results for the connected regime (see the dashed lines in the region of $p > p_c$ in Fig. 8e and f). For the disconnected regime ($p < p_c$), k_{eq} is related to lacunarity which characterises the gaps (i.e. rock bridges) between isolated fractures or clusters. Thus, k_{eq} is insensitive to stress loading that mainly affects fractures. We suspect the equivalent permeability follows

$$k_{eq} = k_m\left(\frac{p_c}{p_c - p}\right)^{\zeta} \quad (p < p_c) \tag{16}$$

where $k_{eq} = k_m$ if $p = 0$, and ζ is an exponent. The value of ζ is derived as follows: if $p_c - p$ is unity, $k_{eq} = k_m p_c^{\zeta} = k_c$, which gives $\zeta = \log_{10}(k_c/k_m)/\log_{10} p_c$. By taking $p_c = 6$ and $\lambda = 1$ (p approaches p_c from below), we also obtain an excellent match to the simulation data (see the dashed lines in the region of $p < p_c$ in Fig. 8e and f). The rationale of determining the number of red links λ is given as follows. When p approaches p_c from below, i.e. p approaches 5, one red link is expected and therefore $\lambda = 1$. When p approaches p_c from above, i.e. p approaches 7, two more traversing flow channels may be added and thus $\lambda = 3$ (see the definition of the percolation parameter in Eq. (3), which indicates that if p increases by 1, one more domain-sized percolating channel is added into the system).

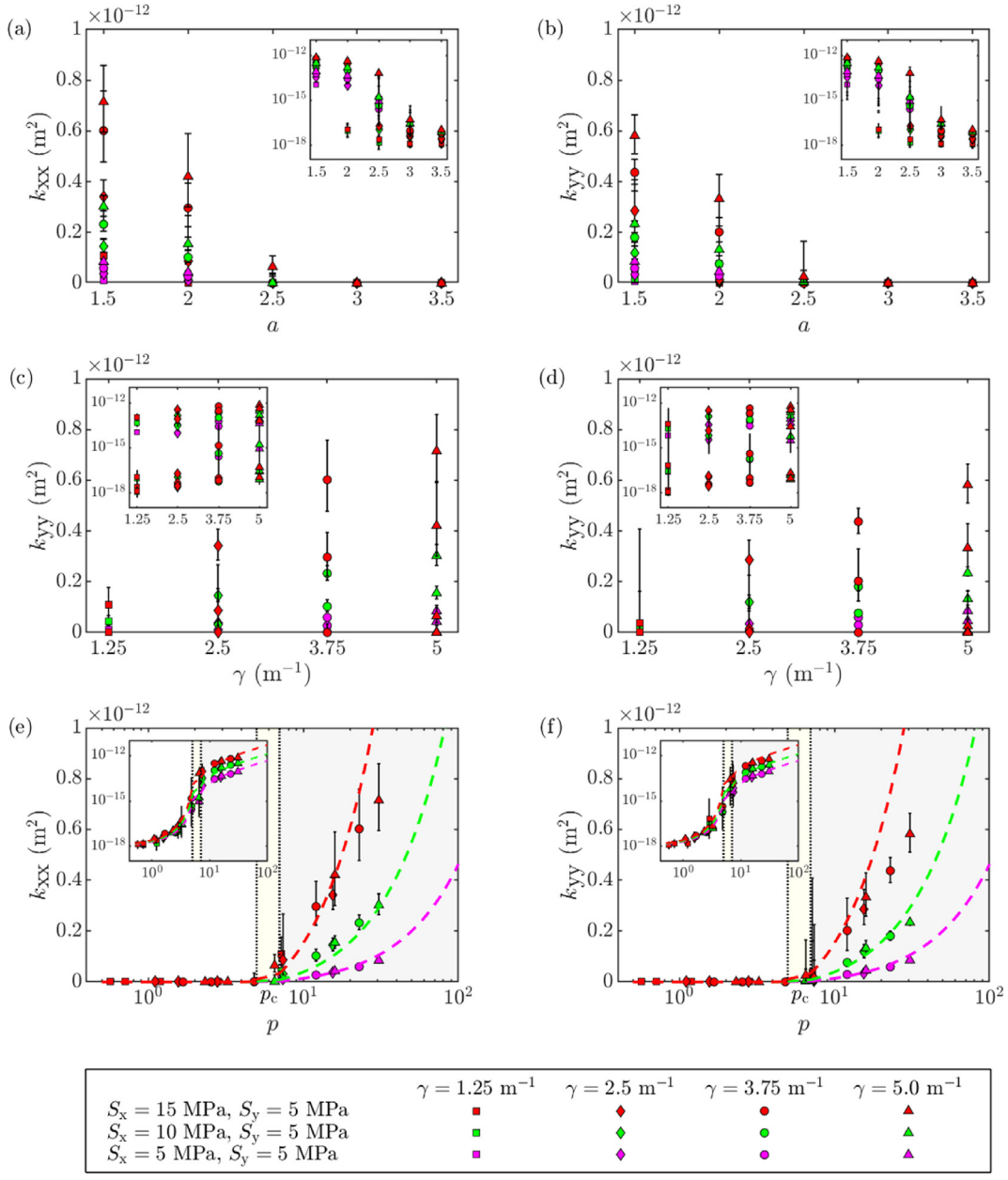

Fig. 8. The equivalent permeability k_{xx} (left panel) and k_{yy} (right panel) of fractured rocks as a function of different geometrical properties, i.e. (a, b) length exponent a, (c, d) fracture intensity γ, and (e, f) percolation parameter p, under different far-field stress conditions. The error bars denote ± 1 standard deviation of the ten realisations. The insets present permeability on the logarithmic scale. In (e, f), the zone bounded by dotted lines corresponds to the percolation threshold $p_c = 6 \pm 1$; and the dashed lines correspond to the analytical solutions, i.e. Eqs. (15) and (16).

For the narrow transitional regime ($p \approx p_c$), we only use a simple interpolation from the solutions of the two neighbouring regimes (see the dashed lines in the region of $p \approx p_c$ in Fig. 8e and f). We have further tested the analytical formulation for a different matrix permeability value ($k_m = 1 \times 10^{-21}$ m^2) in the Appendix (Fig. A6), and a good match to numerical results is also obtained.

5. Discussion and conclusions

In this paper, we presented a systematic investigation into the hydromechanical processes (e.g. stress distribution, fracture closure, shear dilation and fluid flow) in fracture networks of a broad range of geometrical distributions subjected to different stress loading conditions. We examined the variation of hydromechanical properties (e.g. shear displacement, fracture aperture and equivalent permeability) as a function of various geometrical properties (e.g. length exponent a, fracture intensity γ and percolation parameter p). We found that fracture intensity γ is not a good proxy for the hydromechanical behaviour of rock masses, because it poorly (or not at all) indicates the connectivity state of fracture networks (as manifested in Fig. 3 where the networks with the same γ value can have very different connectivity conditions). This observation is consistent with our field characterisation data at the Grimsel Test Site, Switzerland, where a very poor correlation was found between the interval transmissivity (derived from pulse tests) and fracture spacing (fracture intensity measured in one

dimension based on borehole logs) (Brixel et al., 2020a, b). Thus, it is essential to characterise the length distribution of fracture populations in addition to the measurement of fracture intensity (or fracture spacing), as suggested by many previous studies (Bonnet et al., 2001; Davy et al., 2010). The combination of the information of fracture length and intensity permits the calculation of the percolation parameter, which is metric of the fracture network connectivity and serves as an excellent proxy to the hydromechanical behaviour of fractured rocks. This is consistent with past research findings in the literature about the connectivity control on the solid deformation (Zhang and Sanderson, 1998; Harthong et al., 2012; Lei and Gao, 2018) and fluid flow (Hestir and Long, 1990; Bour and Davy, 1997; Renshaw, 1999; de Dreuzy et al., 2001a) of fractured geological media, while our work further advanced the understanding on the mutually-existing, interactively-acting impacts of geometrical connectivity and geomechanical condition on hydrological performance of the system.

Based on our numerical results in Section 4, it seems that the "connectedness" of the fracture system is a prerequisite for notable hydromechanical processes taking effect in fractured rocks. Thus, the system is almost insensitive to the stress loading conditions if it is disconnected. This is because when the fracture network is not percolated, fluid needs to migrate via isolated clusters and the matrix in between them. Hence, the system has an "in series" flow structure (i.e. isolated clusters are linked with each other by matrix), such that the bulk permeability is approximated by the harmonic mean of the permeabilities of different components (de Marsily, 1986) and thus more ruled by the matrix (because it has a low permeability and dominates the harmonic mean). As the system gradually approaches the percolation threshold from below, the size of matrix blocks that form the gaps between isolated clusters is reduced and, therefore, the equivalent permeability increases although the system is still disconnected (Fig. 8e and f). For the connected regime, the system has an "in parallel" flow structure consisting of multiple traversing channels, such that the bulk permeability is approximated by the arithmetic mean of the permeabilities of different components (de Marsily, 1986) and thus controlled by fractures (because they have high permeability and dominate the arithmetic mean). Since fracture aperture (and thus fracture permeability) is dependent on the stress state, the equivalent permeability of fractured rocks also shows a strong dependency on the far-field stress loading. However, it is worth pointing out that the shear-induced aperture enlargement under high stress ratio conditions tends to enlarge the bulk permeability by several times but still within an order of magnitude. We inferred that geomechanical processes tend to exert a secondary-order influence (compared to the first-order role of geometrical connectivity) causing stress-dependent variation of permeability within about one order of magnitude, for which similar permeability variation ranges were also reported in previous studies based on 2D fracture networks (Min et al., 2004b; Baghbanan and Jing, 2008; Latham et al., 2013; Lei et al., 2014). However, more pronounced stress effects might be expected in three-dimensional (3D) fracture systems (Lei et al., 2015, 2017b), which may be of interest for further investigations based on computationally expensive 3D simulations. Further work may also be needed to explore more complicated scenarios of fracture networks, such as anisotropic discontinuity orientations (Lei et al., 2014), multiple domain sizes (Min et al., 2004a), variable initial apertures (Kang et al., 2019), fractal spatial organisations (Davy et al., 2006), and nonlinear mechanical-to-hydraulic aperture correlations (Renshaw, 1995) for testing the generality and sensitivity of the observed phenomena in the current paper.

To conclude, we observed that the geometrical connectivity of fracture networks plays a critical role in the hydromechanical processes in fractured rocks. A well-connected fracture system under a high stress ratio exhibits intense frictional sliding and considerable fracture opening, eventually leading to fast fluid migration and large bulk permeability. Such a connected network is more suppressed for shearing activities under a more isotropic compression, exhibiting a lower permeability compared to that under a high stress ratio loading. A disconnected fracture network is composed of multiple clusters isolated from each other by geomechanically stiffer and hydraulically less permeable matrix rocks, producing mainly fracture closure behaviour and slow fluid flow, with low equivalent permeability insensitive to the far-field stress state. We derived an analytical solution for the relationship between the equivalent permeability of fractured rocks and the percolation parameter of fracture networks, which showed an excellent match to the numerical results. We suggested that the flow through a well-connected system is governed by traversing fractures or clusters "in parallel" and thus the equivalent permeability is sensitive to stress loading (due to the stress dependency of fracture permeability), whilst the flow through a disconnected system is more ruled by matrix, which links isolated clusters "in series", and therefore very insensitive to stress loading. The observation and analysis of interactively superimposed geometrical and geomechanical effects on hydrological properties of fractured geological media as presented in this paper have important implications for understanding heterogeneous subsurface fluid flow and upscaling rock mass permeability.

Declaration of Competing Interest

The authors wish to confirm that there are no known conflicts of interests associated with this publication and there has been no significant financial support for this work that could have influenced its outcome.

Acknowledgments

Qinghua Lei is grateful for the support from Swiss National Science Foundation (Grant No. IZLCZ0_189882). Xiaoguang Wang was partially funded by PRC-CNRS Joint Research Project (Grant No. 5181101856). Ki-Bok Min was partially supported by the Korea-EU Joint Research Support Program of the National Research Foundation of Korea through a grant funded by the Korean Government's Ministry of Science, ICT and Future Planning (Grant No. NRF-2015K1A3A7A03074226) and Research Institute of Energy & Resources, Seoul National University. Support for Jonny Rutqvist was provided by the U.S. Department of Energy under contract No. DE-AC02-05CH11231 to the Lawrence Berkeley National Laboratory.

Appendix A. Supplementary data

Supplementary data to this article can be found online at https://doi.org/10.1016/j.jrmge.2019.12.014.

References

Baghbanan A, Jing L. Hydraulic properties of fractured rock masses with correlated fracture length and aperture. International Journal of Rock Mechanics and Mining Sciences 2007;44(5):704–19.

Baghbanan A, Jing L. Stress effects on permeability in a fractured rock mass with correlated fracture length and aperture. International Journal of Rock Mechanics and Mining Sciences 2008;45(8):1320–34.

Bandis SC, Lumsden AC, Barton NR. Fundamentals of rock joint deformation. International Journal of Rock Mechanics and Mining Sciences & Geomechanics Abstracts 1983;20(6):249–68.

Barton N, Choubey V. The shear strength of rock joints in theory and practice. Rock Mechanics 1977;10(1–2):1–54.

Barton N, Bandis S, Bakhtar K. Strength, deformation and conductivity coupling of rock joints. International Journal of Rock Mechanics and Mining Sciences & Geomechanics Abstracts 1985;22(3):121–40.

Barton CC. Fractal analysis of scaling and spatial clustering of fractures. In: Barton CC, La Pointe PR, editors. Fractals in the Earth Sciences. New York, USA: Plenum Press; 1995. p. 141–78.

Berkowitz B, Balberg I. Percolation theory and its application to groundwater hydrology. Water Resources Research 1993;29(4):775–94.

Berkowitz B. Analysis of fracture network connectivity using percolation theory. Mathematical Geology 1995;27(4):467–83.

Berkowitz B. Characterizing flow and transport in fractured geological media: a review. Advances in Water Resources 2002;25:861–84.

Bonnet E, Bour O, Odling NE, Davy P, Main I, Cowie P, Berkowitz B. Scaling of fracture systems in geological media. Review of Geophysics 2001;39(3):347–83.

Bour O, Davy P. Connectivity of random fault networks following a power law fault length distribution. Water Resources Research 1997;33(7):1567–83.

Bour O, Davy P. On the connectivity of three-dimensional fault networks. Water Resources Research 1998;34(10):2611–22.

Brixel B, Klepikova M, Jalali MR, Lei Q, Roques C, Krietsch H, Loew S. Tracking fluid flow in shallow crustal fault zones: 1. New in situ permeability measurements. Journal of Geophysical Research: Solid Earth 2020a;125(4). https://doi.org/10.1029/2019JB018200. e2019JB018200.

Brixel B, Klepikova M, Lei Q, Roques C, Jalali MR, Krietsch H, Loew S. Tracking fluid flow in shallow crustal fault zones: 2. Insights from cross-hole forced flow experiments in damage zones. Journal of Geophysical Research: Solid Earth 2020b;125(4). https://doi.org/10.1029/2019JB019108. e2019JB019108.

Davy P, Bour O, de Dreuzy J-R, Darcel C. Flow in multiscale fractal fracture networks. In: Cello G, Malamud BD, editors. Fractal analysis for natural hazards. London, UK: Geological Society; 2006. p. 31–45.

Davy P, Le Goc R, Darcel C, Bour O, de Dreuzy J-R, Munier R. A likely universal model of fracture scaling and its consequence for crustal hydromechanics. Journal of Geophysical Research 2010;115(B10):B10411. https://doi.org/10.1029/2009JB007043.

Dershowitz WS, Einstein HH. Characterizing rock joint geometry with joint system models. Rock Mechanics and Rock Engineering 1988;21(1):21–51.

de Dreuzy J-R, Davy P, Bour O. Hydraulic properties of two-dimensional random fracture networks following a power law length distribution: 1. Effective connectivity. Water Resources Research 2001a;37(8):2065–78.

de Dreuzy J-R, Davy P, Bour O. Hydraulic properties of two-dimensional random fracture networks following a power law length distribution: 2. Permeability of networks based on lognormal distribution of apertures. Water Resources Research 2001b;37(8):2079–95.

de Marsily G. Quantitative hydrogeology: groundwater hydrology for engineers. Orlando, USA: Academic Press; 1986.

Goodman RE. Methods of geological engineering. West Publishing Co.; 1976.

Harthong B, Scholtès L, Donzé FV. Strength characterization of rock masses, using a coupled DEM-DFN model. Geophysical Journal International 2012;191:467–80.

Hestir K, Long JCS. Analytical expressions for the permeability of random two-dimensional Poisson fracture networks based on regular lattice percolation and equivalent media theories. Journal of Geophysical Research 1990;95(B13):21565–81.

Jiang C, Wang X, Sun Z, Lei Q. The role of geomechanical processes in organizing flow pathways in a natural fracture network at the percolation threshold. Geofluids 2019;2019:3138972. https://doi.org/10.1155/2019/3138972.

Jin Y, Yuan J, Chen M, Chen KP, Lu Y, Wang H. Determination of rock fracture toughness KIIC and its relationship with tensile strength. Rock Mechanics and Rock Engineering 2011;44(5):621–7.

Kang PK, Lei Q, Dentz M, Juanes R. Stress-induced anomalous transport in natural fracture networks. Water Resources Research 2019;55:4163–85.

Klimczak C, Schultz R, Parashar R, Reeves D. Cubic law with aperture-length correlation: implications for network scale fluid flow. Hydrogeology Journal 2010;18(4):851–62.

Ladanyi B, Archambault G. Simulation of shear behavior of jointed rock mass. In: Proceedings of the 11th US symposium on rock mechanics. Berkeley, USA: American Rock Mechanics Association (ARMA); 1969. p. 105–25.

Lama RD, Vutukuri VS. Handbook on mechanical properties of rocks: testing techniques and resultsvol. 2. Trans Tech Publications; 1978.

Lang PS, Paluszny A, Nejati M, Zimmerman RW. Relationship between the orientation of maximum permeability and intermediate principal stress in fractured rocks. Water Resources Research 2018;54(11):8734–55.

Latham J-P, Xiang J, Belayneh M, Nick HM, Tsang C-F, Blunt MJ. Modelling stress-dependent permeability in fractured rock including effects of propagating and bending fractures. International Journal of Rock Mechanics and Mining Sciences 2013;57:100–12.

Lei Q, Latham J-P, Xiang J, Tsang C-F, Lang P, Guo L. Effects of geomechanical changes on the validity of a discrete fracture network representation of a realistic two-dimensional fractured rock. International Journal of Rock Mechanics and Mining Sciences 2014;70:507–23.

Lei Q, Latham J, Xiang J, Tsang C. Polyaxial stress-induced variable aperture model for persistent 3D fracture networks. Geomechanics for Energy and the Environment 2015;1:34–47.

Lei Q, Wang X. Tectonic interpretation of the connectivity of a multiscale fracture system in limestone. Geophysical Research Letters 2016;43(4):1551–8.

Lei Q, Latham J-P, Xiang J. Implementation of an empirical joint constitutive model into finite-discrete element analysis of the geomechanical behaviour of fractured rocks. Rock Mechanics and Rock Engineering 2016;49(12):4799–816.

Lei Q, Latham J-P, Tsang C-F. The use of discrete fracture networks for modelling coupled geomechanical and hydrological behaviour of fractured rocks. Computers and Geotechnics 2017a;85:151–76.

Lei Q, Wang X, Xiang J, Latham J-P. Polyaxial stress-dependent permeability of a three-dimensional fractured rock layer. Hydrogeology Journal 2017b;25(8):2251–62.

Lei Q, Gao K. Correlation between fracture network properties and stress variability in geological media. Geophysical Research Letters 2018;45(9):3994–4006.

Lei Q, Gao K. A numerical study of stress variability in heterogeneous fractured rocks. International Journal of Rock Mechanics and Mining Sciences 2019;113:121–33.

Liu R, Li B, Jiang Y, Huang N. Review: mathematical expressions for estimating equivalent permeability of rock fracture networks. Hydrogeology Journal 2016;24(7):1623–49.

Long JCS, Billaux DM. From field data to fracture network modeling: an example incorporating spatial structure. Water Resources Research 1987;23(7):1201–16.

Long JCS, Remer JS, Wilson CR, Witherspoon PA. Porous media equivalents for networks of discontinuous fractures. Water Resources Research 1982;18(3):645–58.

Mahabadi O. Investigating the influence of micro-scale heterogeneity and microstructure on the failure and mechanical behaviour of geomaterials. PhD Thesis. Toronto, Canada: University of Toronto; 2012.

Matthäi SK, Belayneh M. Fluid flow partitioning between fractures and a permeable rock matrix. Geophysical Research Letters 2004;31(7):L07602. https://doi.org/10.1029/2003GL019027.

Min K-B, Jing L, Stephansson O. Determining the equivalent permeability tensor for fractured rock masses using a stochastic REV approach: method and application to the field data from Sellafield, UK. Hydrogeology Journal 2004a;12(5):497–510.

Min K-B, Rutqvist J, Tsang C-F, Jing L. Stress-dependent permeability of fractured rock masses: a numerical study. International Journal of Rock Mechanics and Mining Sciences 2004b;41:1191–210.

Munjiza A, Andrews KRF, White JK. Combined single and smeared crack model in combined finite-discrete element analysis. International Journal of Numerical Methods in Engineering 1999;44(1):41–57.

Munjiza A, Andrews KRF. Penalty function method for combined finite-discrete element systems comprising large number of separate bodies. International Journal of Numerical Methods in Engineering 2000;49:1377–96.

Munjiza A. The combined finite-discrete element method. London, UK: Wiley; 2004.

Pollard DD, Aydin A. Progress in understanding jointing over the past century. Geological Society of America Bulletin 1988;100(8):1181–204.

Renshaw CE. On the relationship between mechanical and hydraulic apertures in rough-walled fractures. Journal of Geophysical Research 1995;100:24629–36.

Renshaw CE. Connectivity of joint networks with power law length distributions. Water Resources Research 1999;35(9):2661–70.

Rutqvist J, Stephansson O. The role of hydromechanical coupling in fractured rock engineering. Hydrogeology Journal 2003;11(1):7–40.

Rutqvist J. Fractured rock stress-permeability relationships from in situ data and effects of temperature and chemical-mechanical couplings. Geofluids 2015;15:48–66.

Saeb S, Amadei B. Modelling rock joints under shear and normal loading. International Journal of Rock Mechanics and Mining Sciences & Geomechanics Abstracts 1992;29(3):267–78.

Sanderson DJ, Zhang X. Critical stress localization of flow associated with deformation of well-fractured rock masses, with implications for mineral deposits. Fractures, fluid flow and mineralization. London, UK: Geological Society; 1999. p. 69–81.

Stauffer D, Aharony A. Introduction to percolation theory. Abingdon, UK: Taylor & Francis; 1985.
Tsang C-F, Neretnieks I. Flow channeling in heterogeneous fractured rocks. Review of Geophysics 1998;36(97):275–98.
Wang X, Lei Q, Lonergan L, Jourde H, Gosselin O, Cosgrove J. Heterogeneous fluid flow in fractured layered carbonates and its implication for generation of incipient karst. Advances in Water Resources 2017;107:502–16.
Witherspoon PA, Wang JSY, Iwai K, Gale JE. Validity of cubic law for fluid flow in a deformable rock fracture. Water Resources Research 1980;16(6):1016–24.
Zhang X, Sanderson DJ. Numerical study of critical behaviour of deformation and permeability of fractured rock masses. Marine and Petroleum Geology 1998;15:535–48.
Zhang ZX. An empirical relation between mode-I fracture toughness and the tensile strength of rock. International Journal of Rock Mechanics and Mining Sciences 2002;39:401–6.
Zimmerman RW, Main I. Hydromechanical behavior of fractured rocks. In: Gueguen Y, Bouteca M, editors. Mechanics of fluid-saturated rocks. Elsevier; 2004. p. 363–421.
Zoback MD. Reservoir geomechanics. Cambridge, UK: Cambridge University Press; 2007.

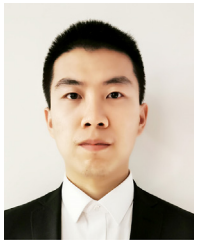

Qinghua Lei is currently a Lecturer and Senior Researcher in Engineering Geology at the Department of Earth Sciences, ETH Zürich, Switzerland. He obtained his bachelor's degree (2009) and master's degree (2012) in Civil Engineering from Tongji University, China, and his PhD (2016) in Rock Mechanics from Imperial College London, UK. Then, he worked as a Post-doctoral Research Associate in Fluid Mechanics at Imperial College London between 2016 and 2018. Dr. Lei is the recipient of the 2019 Rocha Medal from the International Society for Rock Mechanics and Rock Engineering (ISRM), the 2016 NGW Cook PhD Dissertation Award from the American Rock Mechanics Association (ARMA), and the 2015 Rock Mechanics Research Award from the ARMA. Dr. Lei's research covers many cutting-edge topics in the field of rock mechanics and rock engineering, and his research interests include coupled multiphysical processes in geological media, fracture mechanics, fracture patterns, flow and transport in fractured media, statistical physics, seismic wave propagation, interfacial fluid mechanics, slope stability, underground excavation and numerical methods. Dr. Lei is the Secretary General of the ISRM Commission on Thermal-Hydro-Mechanical-Chemical Processes in Fractured Rock and a member of the ARMA Future Leader Committee.